Journal of Materials Chemistry A

Accepted Manuscript

ROYAL SOCIETY OF CHEMISTRY

www.rsc.org/materialsA

Journal Name

ARTICLE

Co–electrodeposited Cu_2ZnSnS_4 thin–film solar cells with over 7% efficiency fabricated via fine–tuning of the Zn content in absorber layers

Received 00th January 20xx,
Accepted 00th January 20xx

DOI: 10.1039/x0xx00000x

www.rsc.org/

Jiahua Tao,[a] Leilei Chen,[a] Huiyi Cao,[a] Chuanjun Zhang,[bc] Junfeng Liu,[a] Yingbin Zhang,[a] Ling Huang,[a] Jinchun Jiang,[ac] Pingxiong Yang[a] and Junhao Chu[*abc]

A simple and cost–effective co–electrodeposition process has been demonstrated to fabricate high–performance Cu_2ZnSnS_4 (CZTS) photovoltaic materials with composition tunability and phase controllability. Here we report a systematic investigation of the Zn(II) concentration on the properties of CZTS thin films and thus the performance of as resulted solar cells. These results indicate that increasing the concentration of Zn(II) linearly increases the Zn content in final composition of CZTS thin films, significantly improves the grain size and morphology of the absorber layers, and consequently improves their photovoltaic properties, especially the response to the medium wavelength. In contrast, upon further increase in the Zn(II) concentration degrades the crystal quality of the absorber layer, the more ZnS phase appears at the surface of CZTS thin film, and forms a rather rough morphology, which is harmful to the photovoltaic performance of the device. When the concentration of Zn(II) is optimized to 30 mM, a power conversion efficiency of 7.23% is achieved, which, to the best of our knowledge, is the highest efficiency for a co–electrodeposited CZTS solar cell with a sputtered CdS buffer layer to date. Our findings offer a promising alternative approach towards the industrialization of CZTS solar cell modules.

Introduction

Kesterite copper zinc tin sulfide (Cu_2ZnSnS_4, CZTS) thin–film solar cells have recently emerged as the leading photovoltaic technologies for the large–scale production because they not only use earth–abundant, nontoxic and inexpensive constituent elements, and but have an ideal band gap of about 1.5 eV with the predicted theoretical maximum efficiencies of over 30%.[1–3] As a result, significant research attention has been mainly focused on the kesterite CZTS material family, and a number of successful solar cells with a range of efficiency levels have been fabricated by a number of research groups. Up to now, the reported highest power conversion efficiencies (PCEs) for pure selenide $Cu_2ZnSnSe_4$ (CZTSe) and mixed sulfo–selenide $Cu_2ZnSn(S,Se)_4$ (CZTSSe) have already reached 11.6% and 12.6% by Mitzi's group,[4,5] while for the pure sulfide CZTS has achieved only 9.2% by Kato *et al*.[6] Although the PCEs of CZTS solar cells are much lower than those of CZTSe and CZTSSe solar cells, the continued development of more environment–friendly commercial application is more suitable for industrial production because they do not require a highly toxic selenization process.

To date, the highest efficiency CZTS solar cell has been obtained using Cu–poor and Zn–rich CZTS absorber layer;[4-6] however, the high level of non–stoichiometry easily forms other competitive secondary phases (e.g., $Cu_{2-x}S$, ZnS, SnS, SnS_2 and Cu_2SnS_3) and defects along with interfacial carrier recombination, largely due to the very small phase stable region of the quaternary CZTS phase,[7,8] which finally causes the photovoltaic performance worse than that of the stoichiometric solar cell. In general, solar cell absorber materials for optical and optoelectronic perform worse in their polycrystalline form because of minority carriers (electrons) recombination at the grain boundaries (GBs); thus, the GBs are essentially important in determining the solar cell characteristics. Therefore, enhancing the crystallinity quality of the absorber layer is an approach for improving the performance of solar cells because it suppresses defect formation, reduces recombination loss, and improves electron collection at the GBs. Consequently, the exquisite controllability over composition and pure phase becomes the top priority in improving the efficiency of CZTS solar cells.

Similar to chalcopyrite Cu(In, Ga)Se_2 (CIGS), kesterite CZTS thin films can be fabricated by both vacuum– and non–vacuum–based deposition techniques.[4–6,9–40] For vacuum–based techniques, co–evaporation and sputtering processes have been successful in preparing CZTS solar cells, and have achieved PCEs of 8.4%[18] and 9.2%,[6] respectively. One advantage of these vacuum techniques is the versatility afforded by the integration of multiple evaporation or sputtering sources, thereby providing good control over the film

[a] *Key Laboratory of Polar Materials and Devices, Ministry of Education, Department of Electronic Engineering, East China Normal University, Shanghai 200241, China. E–mail address: jhchu@mail.sitp.ac.cn (JH. Chu)*
[b] *National Laboratory for Infrared Physics, Shanghai Institute of Technical Physics, Chinese Academy of Sciences, Shanghai 200083, China*
[c] *Shanghai Center for Photovoltaics, Shanghai 200083, China*
† Footnotes relating to the title and/or authors should appear here.
Electronic Supplementary Information (ESI) available: Experimental, Cyclic voltammetry, Amperometric I–t, Composition analysis, Surface and cross–sectional SEM images, XRD spectra and ln(J–GV) versus V–RJ. See DOI: 10.1039/x0xx00000x

composition and phase profile. However, vacuum conditions require an evacuated confined space, which is not suitable for the cost–effective deposition of uniform thin films over large–area substrates. They also generally suffer from a relatively slow throughput, low materials use and considerable energy expenditure to heat or sputter from the target sources. To overcome these limitations, non–vacuum–based techniques are being developed in a reduction in the manufacturing cost of CZTS absorber layers. So far, the highest PCEs for CZTSSe solar cells containing toxic selenium were achieved by a hydrazine–based hybrid slurry approach.[5] However, since the hydrazine has attained a somewhat infamous reputation in this field based on its hepatotoxic, carcinogenic and explosive, significant safety issues should be taken into account when dealing with it during film formation.

As opposed to the vacuum–based and other non–vacuum–based techniques, electrodeposition provides the simplicity, high material utilization, facile control of the precursor ratios and room–temperature to prepare large–area and uniform CZTS precursors for low–cost and high–efficiency solar cells. This process can be further divided into two categories: (i) electrodeposited stacked elemental layers[9–11] and (ii) co–electrodeposited layer.[12–16] Current issue for electrodeposited stacked CZTS precursor is the morphology of Sn precursor was very rough compared to the other elemental precursors.[11] In addition, the poor morphology of CZTS is due to non–uniform nucleation of Zn precursor.[11] Hence co–electrodeposition of Cu–Zn–Sn–S precursors is preferred.[12,13,16,29] Ahmed et al. in 2012 reported a CZTS–based solar cell with a PCE of 7.3%: the absorber layer was prepared by sulfurization of electrodeposited Cu/Zn/Sn metallic stack precursor films at 585 °C for 12 min.[9] Recently, an outstanding PCE of 7.99% has been reached by stacked electrodeposited CZTS absorber layers from sulfurization of preheated Cu/Zn/Sn metallic stack precursor films.[10] Our group has recently demonstrated that the Cu content and thicknesses of co–electrodeposited CZTS thin films can be easily tuned by varying the electrodeposition time and the concentration of Cu(II) in the precursor solution, enhanced the device's PCE from 6.6% to 7.1%.[12,13] Furthermore, we have fabricated a co–electrodeposited CZTS solar cell with an area of 0.20 cm^2 bigger than the previously electrodeposited stacked cell with an area of 0.03 cm^{-2}.[13,10] Indeed, co–electrodeposition process is based upon an instantaneous synthesis of a Cu–Zn–Sn–S precursor at room temperature using a non–toxic and low–cost precursor solution. Moreover, the influence of Zn(II) concentrations in the precursor solutions on the growth process and microstructure of co–electrodeposited CZTS thin films, and the photovoltaic characteristics of their solar cell devices have not yet been understood completely. In this work, therefore, the remarkable effects of Zn(II) concentrations on the microstructure of CZTS absorbers and the photovoltaic characteristics of these CZTS solar cell devices have been investigated.

Experimental

Cyclic voltammetry tests were measured and amperometric I–t curves were recorded at room temperature without stirring using a CHI660D electrochemical workstation (CH Instrument, USA, Figure S1). CZTS thin films were deposited on molybdenum coated glass substrates (3.0×2.5 cm^2, Mo/glass) by using the modified co–electrodeposition method as detailed in our previous works.[12,13] The precursor solutions were first made by simultaneously dissolving 10 mM $CuSO_4 \cdot 5H_2O$, 5–40 mM $ZnSO_4 \cdot 7H_2O$, 20 mM $SnSO_4 \cdot 2H_2O$, 20 mM tartaric acid, 100 mM trisodium citrate and 10 mM sodium thiosulfate in aqueous solutions (200 mL) at room temperature. This solution system is safe, simple and easy to use. The concentration of $ZnSO_4 \cdot 7H_2O$ was systematically varied from 5.0 to 40 mM at an interval of 10 mM to deposit Cu–Zn–Sn–S precursor films. These precursor films were then annealed with elemental S in a rapid thermal process (RTP) furnace at temperature of 570 °C for 15 min to form CZTS thin films. The sulfurized CZTS thin films were denoted CZTS(05), CZTS(10), CZTS(20), CZTS(30) and CZTS(40) depending on the Zn(II) concentration.

The structural properties of the prepared CZTS thin films were analyzed by X–ray diffraction (XRD) using a Bruker D8 Discover diffractometer with Cu Kα radiation (λ=1.5406 Å). Raman measurements were performed using the 532 nm line of an Ar^+ laser with 50 mW, and the 325 nm line of a He–Cd laser with 0.5 mW as excitation sources. Infrared reflection absorption spectroscopy (IR) measurements were performed using a Fourier Transform infrared spectrometer (Bruker Vertex 80 V). X–ray photoelectron spectroscopy (XPS) measurements were performed using a PHI 5000C ESCA System with Mg Kα source at 14.0 kV and 25 mA. All the binding energies were referenced to the contaminant C 1s peak at 284.6 eV of the surface adventitious carbon. The morphologies and chemical compositions were examined using a PhilipsS360 scanning electron microscope (SEM) attached to an energy–dispersive X–ray spectroscope (EDS, accelerating voltage of 20 kV, measured area of 20×20 μm^2). The element components were obtained as average values between two regions at the surface of the films.

The CZTS absorber layers were processed to complete solar cell devices with a conventional structure of an AZO/i–ZnO/CdS/CZTS/Mo/glass (without an antireflection layer), as presented in Figure S2. The CdS (~150 nm), i–ZnO (~50 nm) and Al–doped ZnO (AZO, ~700 nm) were subsequently deposited by radio–frequency (RF)–magnetron sputtering, respectively, giving a standard CZTS device structure with a device area of approximately 0.20 cm^2, as defined by mechanical scribing. The current density–voltage (J–V) characteristics of CZTS solar cells were performed using a continuous light solar cell performance tester system in the dark at 25 °C and under simulated air mass AM1.5 G (100 mW cm^{-2}) using a solar simulator (Xe lamp, Newport). External quantum efficiency (EQE) measurements were performed by a single source illumination system (Qtest Station 1000AD EQE) combined with a monochromator. A calibrated Si–cell was used as reference for the J–V as well as for the EQE measurements.

Results and discussion

Table 1. Chemical compositions of the sulfurized CZTS thin films as a function of the concentration of Zn(II) in precursor solutions.

Sample ID	Elemental component (at %)				Composition ratio		
	Cu	Zn	Sn	S	Cu/(Zn+Sn)	Zn/Sn	S/Metal

CZTS(05)	23.87	12.43	12.03	51.67	0.98	1.03	1.07
CZTS(10)	23.18	14.37	11.22	51.23	0.91	1.28	1.05
CZTS(20)	21.79	15.01	11.87	51.33	0.81	1.26	1.05
CZTS(30)	21.15	15.75	12.08	51.02	0.76	1.30	1.04
CZTS(40)	19.97	17.11	11.27	51.65	0.70	1.52	1.07

The chemical compositions of the Cu–Zn–Sn–S precursor films and the sulfurized CZTS films were determined by EDS analyses, as they are summarized in Table S1, Table 1 and Figure S3. All precursor films are Cu-poor and Zn-rich compositions with the ratios of Cu/(Zn+Sn) <0.91 and Zn/Sn >1.00 similar to those described for previous record devices.[5,9,34,39,40] In the fabrication process of CZTS thin films, the content of sulfur (S/Metal ratio of <0.2) in the co–electrodeposited Cu–Zn–Sn–S precursors is critical processing for the formation of high quality thin films because the presence of sufficient sulfur in the precursors can avoid some deterioration in the morphology of the sulfurized thin films caused by volume expansion during the sulfurization process.[21] After sulfurization of these precursors, all sulfurized CZTS thin films show slightly S–rich with S/metal ratio of >1, which indicates that sulfur is sufficiently incorporated into CZTS thin films. It is beneficial to decrease the amounts of sulfur vacancies and improve the crystalline quality of CZTS thin films.[16,29] In addition, the ratios of Cu/(Zn+Sn) and Zn/Sn of the sulfurized CZTS thin films are approximately proportional to those of the precursor thin films. However, it is observed evidently that the ratios of Cu/(Zn+Sn) and Zn/Sn increase slightly in all sulfurized thin films in comparison with all precursor thin films, suggesting the severe loss of Sn due to high volatility of tin sulfide during sulfurization process.[29] It is clear that the content of Zn linearly increases while that of Cu slightly decreases with increasing the concentration of Zn(II), which reveals that the amount of Zn in the final thin film can be approximately controlled by varying the Zn(II) concentration of the precursor solution. As shown in Figure S1a, the reduction potential of Zn shifts toward less positive potential with increasing the Zn(II) concentration, indicating that the content of Zn in the CZTS thin film relatively increases with increasing the Zn(II) concentration. The compositions of all thin films are the Cu/(Zn+Sn) ratio of <1.0 and Zn/Sn ratio of >1.0, respectively, yielding the Cu–poor and Zn–rich compositions, close to those previously reported values for high performance absorbers.[4–6,9-13,22,27,28,33,34,39,40] Thus, a range of Zn–rich and Cu–poor CZTS thin films may be deposited using the co–electrodeposition method, and the chemical composition of the sulfurized thin films can be controlled fairly well by tuning the concentration of the precursor solution. The continued refinement of compositional and phase control may allow this method to compare with vacuum–based approaches for both the large–scale film production and the exploration of their properties in order to further advance our understanding and application of this material system.

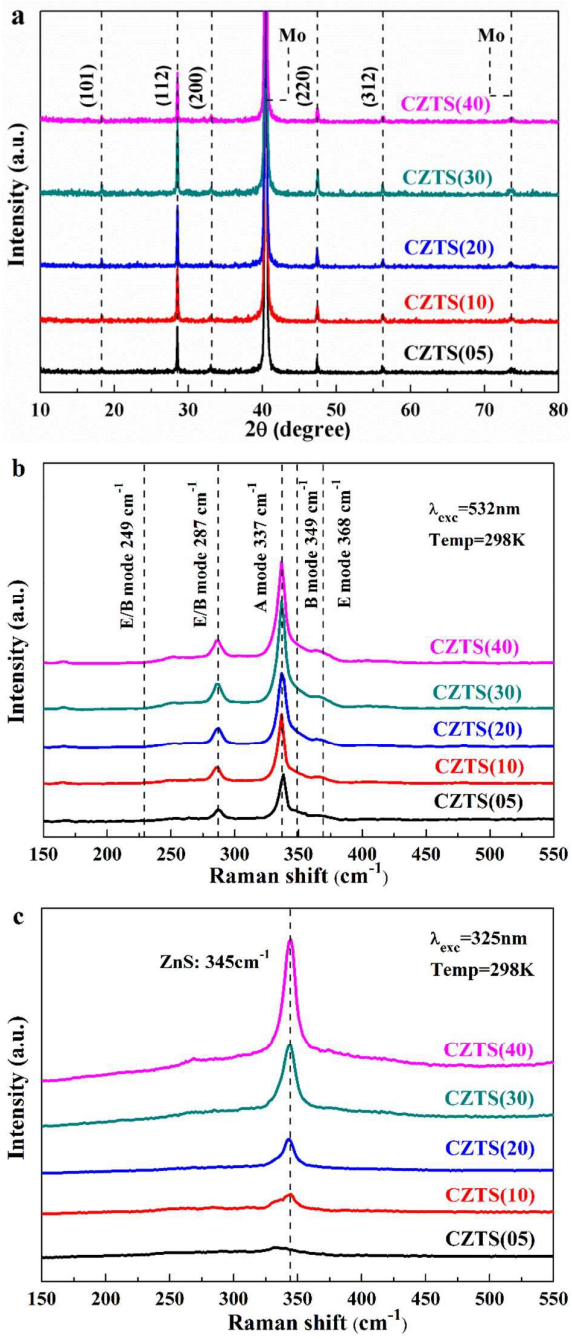

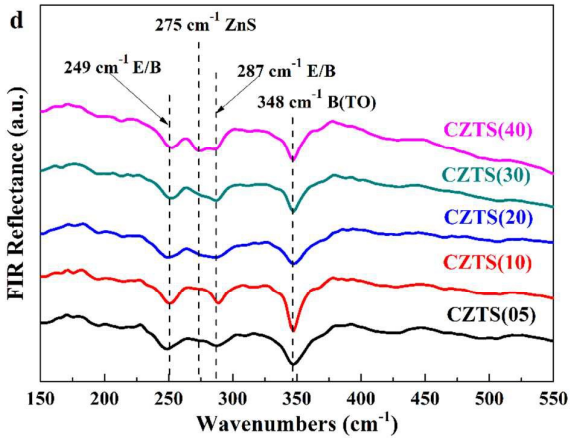

Figure 1. (a) XRD patterns, (b, c) Raman spectroscopy with excitation wavelengths of 532 nm, 325 nm, and (d) FIR spectra patterns of the sulfurized CZTS thin films as a function of Zn(II) concentration.

Figure 1a shows the XRD patterns of co–electrodeposited CZTS thin films as a function of Zn(II) concentrations (5, 10, 20, 30 and 40 mM). Regardless of the Zn(II) concentration, the XRD patterns of all the films are consistent with the kesterite structure of CZTS (JCPDS 26–0575).[9–13] Interestingly, the intensity of the (112) peak increases and then drops with increasing Zn(II) concentration. These changes indicate an improvement in the crystallinity of the CZTS thin films with an increase in the certain amount of Zn in final CZTS thin films (see Table 1), which can presumably be attributed to the increase in grain size, as observed in the surface and cross–sectional SEM images of CZTS(05) (Figure 3a, 3f), CZTS(10) (Figure 3b, 3g), CZTS(20) (Figure 3c, 3h), and CZTS(30) (Figure 3d, 3j). Moreover, no secondary phases could be identified from the XRD patterns of the five samples, the presence of ZnS and Cu_2SnS_3 impurity phases cannot be excluded since their reflexes overlap with those of CZTS and therefore, cannot be distinguished by XRD. Reflexes at 28.53°, 47.33° and 56.18° confirm unambiguously the CZTS phase. Besides, it is reported that the enthalpy of formation of ZnS is relatively lower than those of other binary sulfide compounds,[7] which suggests that ZnS phase easily forms during the sulfurization process. Thus, it is very challenging in producing Cu–poor and Zn–rich CZTS thin films with fine control over composition and pure phase by tuning the Zn(II) concentration in the precursor solution.

In order to further investigate the formation and phase purity of CZTS thin films, Raman scattering spectroscopy with a 532 nm excitation wavelength (red spectra) was taken (Figure 1b). All peaks of all films are assigned to the vibration modes of kesterite CZTS, with the major peaks (A_1 symmetry mode) at 337 cm^{-1} and 287 cm^{-1}.[12,13] Several weaker peaks at around 249 cm^{-1}, 349 cm^{-1} and 368 cm^{-1} are identified with B/E, B(TO) and B(LO) symmetry CZTS modes, respectively, similar to results reported in the literature.[12,13] Most importantly, no significant indication of phase separation for Cu_2SnS_3 at 318 cm^{-1},[13] ZnS at 345 cm^{-1},[13] and $Cu_{2-x}S$ at 475 cm^{-1},[13,29] can be detected by either Raman or XRD measurements. As the Zn(II) concentration increases, the intensity of A_1 mode firstly increases and then decreases, as suggested by the XRD results (Figure 1a). Moreover, in order to enhance detection selectivity and sensibility to the potential presence of ZnS phase, Raman scattering measurements with the energy of light source (325 nm He–Cd laser) are very close to the resonance condition of the ZnS (ca. 3.7 eV). The ZnS secondary peak at 345 cm^{-1} is easily observed only when we used the 325 nm laser, as shown in Figure 1c. As the Zn(II) concentration increases, the intensity of ZnS peak increases. This change signifies an increase in the amount of the ZnS phase, which is consistent with the increase in the Zn content of CZTS thin films in combination with the compositions in Table S1 and Table 1. But the secondary phase of ZnS with a wide band gap in the bulk of CZTS thin films can reduce the active area to generate the electron–hole pairs and current collection while at the interfaces it can increase the series resistance, reduce the fill factor and short circuit current of the device. Furthermore, FIR spectroscopy is also a useful technique to explore the infrared active mode behavior of CZTS thin films. Figure 1d shows the infrared–active B/E and B(TO) modes of kesterite CZTS phase at 249 cm^{-1}, 287 cm^{-1} and 348 cm^{-1}, and mode at 275 cm^{-1} assignable to cubic ZnS phase, which are close to those found in Raman scattering spectrum in Figure 1b. Moreover, these vibrational modes observed in the Raman scattering and FIR spectra are in excellent agreement with the calculated values of CZTS kesterite phase. As a result, the single–phase CZTS thin films can be effectively achieved by adjusting the Zn(II) concentration.

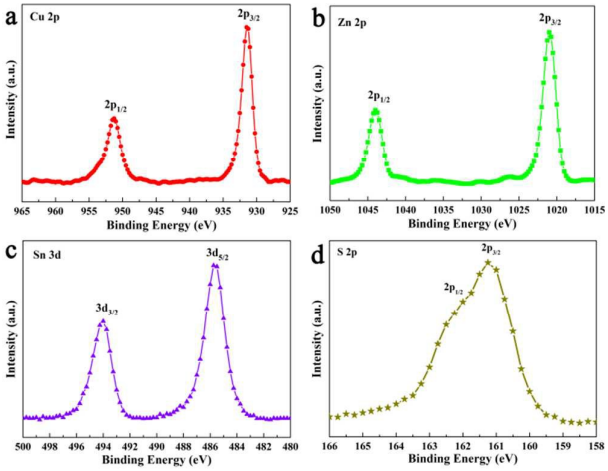

Figure 2. High–resolution XPS spectra of (a) Cu 2p, (b) Zn 2p, (c) Sn 3d and (d) S 2p for the CZTS(30) thin film recorded at room temperature.

High–resolution X–ray photoelectron spectroscopy (XPS) analysis was performed to investigate the oxidation states of CZTS(30) thin film' surface elements (Figure 2). The XPS survey spectrum identified the presence of Cu, Zn, Sn and S. In the Cu 2p spectrum, two characteristic Cu 2p core level spectra clearly shows binding energy values for the Cu $2p_{1/2}$ and Cu $2p_{3/2}$ peaks at 952.4 eV and 932.6 eV, respectively, with a peak splitting of 19.8 eV, indicating the presence of Cu(I). The Zn $2p_{1/2}$ and $2p_{3/2}$ peaks located at 1045 eV and 1022 eV show a peak separation of 23 eV, revealing the formation of Zn(II) state. In the Sn 3d core level, $3d_{3/2}$ and $3d_{5/2}$ peaks are located at 494.5 eV and 486.1 eV, respectively, corresponding to the Sn(IV) state with a characteristic binding energy of 8.4 eV. Finally, the S $2p_{1/2}$ and $2p_{3/2}$ peaks in the spectra are located at 162.5 eV and 161.3 eV with a peak splitting of 1.2 eV, consistent with the presence of sulfide specie. Thus, these results are

consistent with the expected values.[13]

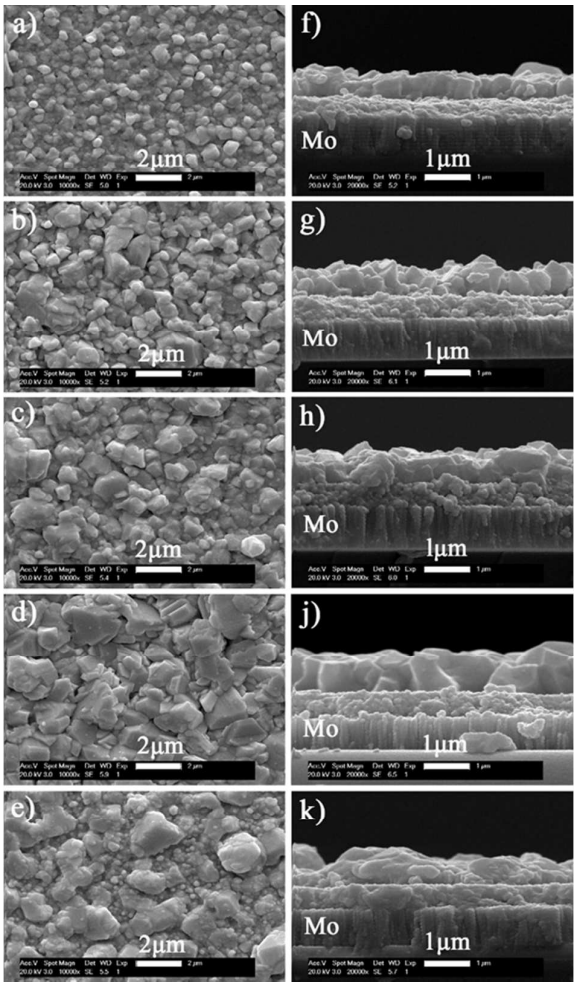

Figure 3. Surface and cross sectional SEM images of the sulfurized CZTS thin films: (a, f) CZTS(05), (b, g) CZTS(10), (c, h) CZTS(20), (d, j) CZTS(30) and (e, k) CZTS(40).

Figure 3 shows the morphologies of CZTS thin films derived from co–electrodeposited Cu–Zn–Sn–S precursors with various Zn(II) concentrations. Overall, all thin films are dense and pinhole–free, without obvious voids at the CZTS/Mo interface. Moreover, the MoS_2 layer is not observed between the CZTS thin film and the Mo back contact, suggesting the MoS_2 layer thickness is substantially thinner than previously reported devices.[21,22,25,26] Interestingly, we observed that increasing the Zn(II) concentration from 5 to 30 mM, the grain size becomes relatively larger, the film surface is denser, and isolated grains with large size and well–defined boundaries are formed, as evident in Figure 3a–3d, as it has been shown by the XRD and Raman results. This implies the significant improvement of the grain size of CZTS thin films. Large grains generally benefit device performance due to less opportunity for recombination of photogenerated carriers at the grain boundaries.[9,12,13,34] However, when increasing the Zn(II) concentration to 40 mM, CZTS(40) thin film has larger micron sized grains and while presents a rather rough surface morphology. The relatively rough surface may be deleterious to the formation of CZTS/CdS heterojunction and thus increase the interface combination of charge carriers.[10,12,13,] As shown in Figure 3f–3j, it is clear that all CZTS thin films consist of a distinct bilayer structure: a large–grain top layer and a small–grain bottom layer. The large grains seen on the top view SEM image do not extend vertically through the absorber layer. The small grains are generally deleterious to device performance due to increased opportunity for recombination at grain boundaries and/or decreased carrier mobility.[13] Hence, further optimization of the composition of CZTS precursor (e.g., deposition potential, deposition time, concentration, pH and additives) and sulfurization conditions (e.g., temperature, pressure and time) is crucial to fabricate homogeneous CZTS absorber layers with large densely packed grains for the fabrication of high–efficiency solar cell devices.

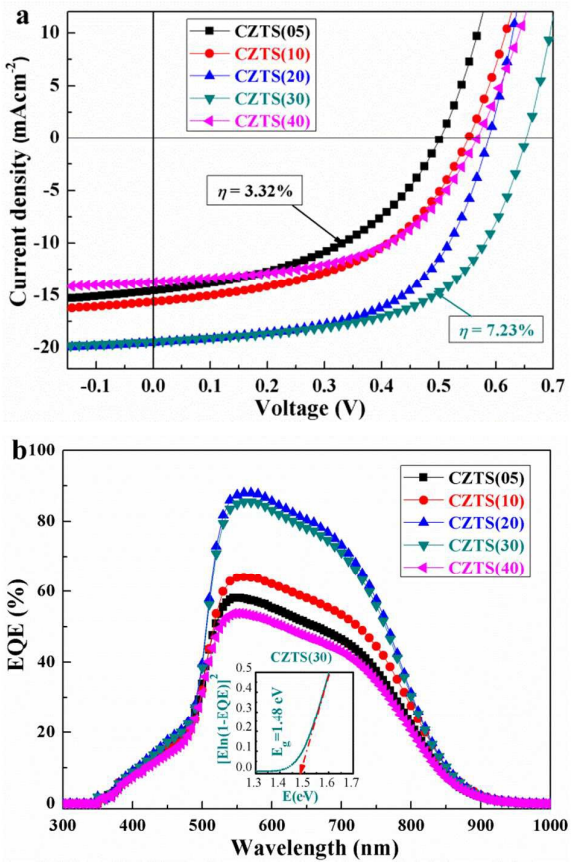

Figure 4. (a) Current density–voltage (J–V) characteristics of CZTS solar cell devices measured under AM 1.5 simulated illumination, (b) EQE measurements of the corresponding CZTS solar cell devices.

Table 2. Device parameters for CZTS solar cell devices as a function of the concentration of Zn(II) in precursor solutions.

Cells	PCE [%]	V_{oc} [mV]	J_{sc} [mA cm^{-2}]	FF [%]	R_s [Ω cm^2]	R_{sh} [Ω cm^2]	A	J_o [mA cm^{-2}]
CZTS(05)	3.32	501.7	14.5	45.5	11.9	419.5	4.96	9.2×10^{-2}
CZTS(10)	4.19	551.3	15.5	48.8	10.7	486.7	3.01	3.1×10^{-3}
CZTS(20)	6.57	592.3	19.5	57.5	6.7	698.6	2.76	1.1×10^{-4}
CZTS(30)	7.23	636.0	19.2	58.7	5.4	737.4	1.75	3.1×10^{-5}

CZTS(40)	4.14	566.9	13.7	53.3	11.7	365.1	2.16	1.7×10^{-4}

To better understand the influence of Zn(II) concentration on the photovoltaic properties of CZTS thin films, complete thin–film solar cell devices with the structure of AZO/i–ZnO/CdS/CZTS/Mo/Glass were fabricated. Figure 4a and Table 2 show the current density–voltage (J–V) characteristics of CZTS solar cell devices measured under AM 1.5G solar illumination at 100 mW cm^{-2}. The device efficiency drastically improves from 3.32% to 7.23%; one of the devices obtained from CZTS(30) absorber layer has the best efficiency of 7.23%, which is among the highest reported to date for co–electrodeposited CZTS solar cells. The simultaneous improvement in the short–circuit current density (J_{sc}), open–circuit voltage (V_{oc}) and fill factor (FF) may originate from reduced recombination loss or increased absorption of photons, or indeed a combination of both, probably related to the observation of the high–quality microstructure with large grains (>1 μm). This change in the crystallinity of CZTS can influence the GBs in the absorber layer, as seen in SEM and Raman analysis (see Figure 3 and Figure 1). The significant decrease in the series resistance (R_s from 11.9 to 5.4 Ω cm^2) leads to a rise in the FF value as well as an increase in the J_{sc} (Table 2). Generally, the R_s is attributed to the contact and material resistances from the Mo back contact, CZTS absorber layer, Mo/CZTS interface, CZTS/CdS interface and AZO window layer. However, the AZO/i–ZnO/CdS layers in the our devices were prepared by identical processes, without undergoing the different Zn(II) concentrations in precursor solutions. Therefore, the distinct decrease in R_s with increasing Zn(II) concentration can be unambiguously assigned to the decreasing the thickness of small–grain bottom layer and the relatively smooth surface, as shown in Figure 3. Moreover, the V_{oc} significantly improves from 501.7 to 636.0 mV. It is well known that $V_{oc} = AkT/q\ln(J_{sc}/J_o)$, where A, kT/q and J_o are the diode ideality factor, thermal voltage and reverse saturation current, respectively. Table S2 show that J_o values of CZTS(05, 10, 20 and 30) solar cells are 9.2×10^{-2}, 3.1×10^{-3}, 1.1×10^{-4} and 3.1×10^{-5} mA cm^{-2}, respectively. V_{oc} is inversely proportional to J_o, and thus CZTS(30) solar cell has the biggest V_{oc} value. The A of CZTS solar cells has also improved from 4.96 to 1.75 with the increase in Zn(II) concentration, consistent with the improvement in V_{oc} that suggests less recombination in the space–charge region (either interface or bulk). Meanwhile, the change of the A from larger than 3 to lower than 2 means the recombination mechanisms alteration, which might be caused by the change in composition and microstructure of the CZTS absorbers (Table 1, Figure 1 and Figure 3). When compared to the CZTS solar cell,[18] the best efficiency in the our device is limited by relatively low FF mainly due to high R_s (5.4 Ω cm^2), high A (2.02) and low J_o (3.1×10^{-5} mA cm^{-2}). The addition of a Ni/Al grid and standard MgF_2 antireflection coating might increase the PCE up to around 8%. However, the PCE of CZTS(40) solar cell only yields 4.14% with J_{sc}=13.7 mA cm^{-2}, V_{oc}=566.9 mV and FF=53.3%. A low shunt resistance of 365.1 Ω cm^2 and a high series resistance of 11.7 Ω cm^2 limit the overall device performance, resulting in a substantial loss in FF (53.3%), which could be related to the smaller CZTS grains, the more ZnS with a wide band gap and relatively rough surface morphologies as indicated in the SEM and Raman results (Figure 2c and Figure 3e). Therefore, further tuning the precursor composition (eg., Cu(II) and Sn(II) ions) may need to be more finely controlled to fabricate high crystalline quality, phase purity and smooth surface of CZTS absorber layers in order to further increase the device performance.

To confirm the accuracy of the J–V measurements, the external quantum efficiency (EQE) curves of the corresponding CZTS solar cell devices were measured; these are compared in Figure 4b. The calculated J_{sc} values obtained by integrating the product of the EQEs are 14.3, 15.7, 19.3, 19.7 and 13.9 mA cm^{-2} for CZTS(05–40) solar cells, respectively, which is in good agreement with the directly measured J_{sc} values from the J–V characteristics (Table 2). The wavelengths below ~500 nm (blue collection) are slightly poorer than those reported by others[5,9,18] due to slightly thicker CdS thicknesses. Compared to the electrodeposited stacked CZTS solar cell (PCE=7.3%, J_{sc}=22 mA cm^{-2}),[9] short wavelength loss occurs at the front of the CZTS(30) solar cell (PCE=7.23%, J_{sc}=19.2 mA cm^{-2}) due to the absorption of short wavelength region in the sputtered CdS buffer layer, this effect is compensated by enhanced medium wavelength (520–750 nm) response, as shown in Figure S6. This is probably due to the fact that the sputtered CdS thin film has relatively good quality and high transmittance in Figure S5. Moreover, CdS thin films deposited on both glass substrate and CZTS/Mo/glass substrate exhibit the polycrystalline diffraction peaks corresponding to hexagonal H(002)/C(111) and H(004)/C(222) planes (see Figure S5). As the Zn(II) concentration increases from 5 to 30 mM, the maximum EQEs of the devices at ~560 nm increase from ~52% to ~85%, which could occur if interface recombination at medium wavelength (520–800 nm) has been improved. This improvement is consistent with the trend observed in J_{sc} (Table 2), which can be explained by the fact that the absorber layer from a high Zn(II) concentration results in a high quality CZTS: larger grains with less grain boundaries. However, the EQEs dramatically drop off in longer wavelength region from 700 to 900 nm. This decay is most likely caused by poor minority carrier diffusion length and/or insufficient penetration of the depletion width into the absorber.[5,18,27] The band gap of the CZTS(30) absorber layer is determined to be 1.48 eV by fitting a plot of $[E\ln(1-\mathrm{EQE})]^2$ vs. E near the band edge, as shown in the inset of Figure 4b.

Conclusions

In conclusion, we have investigated that controlling the Zn(II) concentration of the precursor solutions used to fabricate the CZTS thin films has a significant effect on some key properties of the absorber layers of our solar cell devices. These results suggest that the increase in Zn(II) concentration from 5 to 30 mM enhances grain growth in the CZTS absorber layer, accordingly reduces the series resistance, and hence improves the device efficiency from 3.32% to 7.23% by simultaneously enhancing the short–circuit current density, open–circuit voltage and fill factor. This is the highest efficiency reported so far for a CZTS solar cell prepared by co–electrodeposition method. However, the further increase of the Zn(II) concentration to 40 mM, degrades the CZTS absorber's crystallinity, exhibits the relatively rough surface morphology, and has more ZnS phase, which is detrimental to photovoltaic performance. These findings offer a better understanding of the growth process of the CZTS absorber layers, which are critical for

the precise control and adjustment of the composition, phase, structure and morphologies to facilitate high–efficiency CZTS solar cells.

Acknowledgements

Authors thank Dr. Lin Sun, Dr. Zhigao Hu and Dr. Fangyang Liu for the technical supports. This work was financed by Major State Basic Research Development Program of China (Grant No. 2013CB922300), the National Science Foundation of China (Grant no. 61474045) and Knowledge Innovation Program of the Chinese Academy of Sciences (Grant No. Y2K4401DG0).

Notes and references

1 B. Bob, B. Lei, C.H. Chung, W. Yang, W.C. Hsu, H.S. Duan, W.W.J. Hou, S.H. Li and Y. Yang, Adv. Energy Mater., 2012, 2, 504–522.
2 M.A. Green, K. Emery, Y. Hishikawa, W. Warta and E.D. Dunlop, Prog. Photovolt: Res. Appl., 2015, 23, 1–9.
3 W. Shockley and H.J. Queisser, Adv. Energy Mater., 2011, 1, 732–735.
4 Y.S. Lee, T. Gershon, O. Gunawan, T.K. Todorov, T. Gokmen, Y. Virgus and S. Guha, Adv. Energy Mater., 2014, 5, 1401372.
5 W. Wang, M.T. Winkler, O. Gunawan, T. Gokmen, T.K. Todorov, Y. Zhu and D.B. Mitzi, Adv. Energy Mater., 2014, 4, 1301465.
6 T. Kato, H. Hiroi, N. Sakai, S. Muraoka and H. Sugimoto, Eur. Photovoltaic Sol. Energy Conf., Proc. Int. Conf., 2012, 2236–2239.
7 S. Chen, A. Walsh, X.G. Gong and S.H. Wei, Adv. Mater., 2013, 25, 1522–1539.
8 S. Chen, J.H. Yang, X.G. Gong, A. Walsh and S.H. Wei, Phys. Rev. B: Condens. Matter., 2010, 81, 245204.
9 S. Ahmed, K.B. Reuter, O. Gunawan, L. Guo, L.T. Romankiw and H. Deligianni, Adv. Energy Mater., 2012, 2, 253–259.
10 F. Jiang, S. Ikeda, T. Harada and M. Matsumura, Adv. Energy Mater., 2014, 4, 1301381.
11 J.J. Scragg, D.M. Berg and P.J. Dale, J. Electroanal. Chem., 2010, 646, 52–59.
12 J. Tao, K. Zhang, C. Zhang, L. Chen, H. Cao, J. Liu, J. Jiang, L. Sun, P. Yang and J. Chu, Chem. Commun., 2015, 51, 10337–10340.
13 J. Tao, J. Liu, L. Chen, H. Cao, X. Meng, Y. Zhang, C. Zhang, L. Sun, P. Yang and J. Chu, Green Chem., 2015, DOI: 10.1039/c5gc02057c.
14 A. Ennaoui, M. Lux–steiner, A. Weber, D. Abou–Ras, I. Kotschau, H.W. Schock, R. Schurr, A. Holzing, S. Jost, R. Hock, J. Schulze and A. Kirbs, Thin Solid Films, 2009, 517, 2511–2514.
15 K.V. Gurav, S.W. Shin, U.M. Patil, M.P. Suryawanshi, S.M. Pawar, M.G. Gang, S.A. Vanalakar, J.H. Yun and J.H. Kim, J. Alloys Comp., 2015, 631, 178–182.
16 J. Tao, J. He, K. Zhang, J. Liu, Y. Dong, L. Sun, P. Yang and J. Chu, Mater. Lett., 2014, 135, 8–10.
17 H. Katagiri, K. Jimbo, W.S. Maw, K. Oishi, M. Yamazaki, H. Araki and A. Takeuchi, Thin Solid Films, 2009, 517, 2455–2460.
18 B. Shin, O. Gunawan, Y. Zhu, N.A. Bojarczuk, S.J. Chey and S. Guha, Prog. Photovolt: Res. Appl., 2013, 21, 72–76.
19 Q. Guo, G.M. Ford, W.C. Yang, B.C. Walker, E.A. Stach, H.W. Hillhouse and R. Agrawal, J. Am. Chem. Soc., 2010, 132, 17384–17386.
20 X. Liu, F. Zhou, N. Song, J. Huang, C. Yan, F. Liu, K. Sun, J.A. Stride, X. Hao and M.A. Green, J. Mater. Chem. A, 2015, 3, 23185–23193.
21 Z. Su, K. Sun, Z. Han, H. Cui, F. Liu, Y. Lai, Y. Lai, J. Li, X. Hao, Y. Liu and M.A. Green, J. Mater. Chem. A, 2014, 2, 500–509.
22 F. Liu, F. Zeng, N. Song, L. Jiang, Z. Han, Z. Su, C. Yan, X. Wen, X. Hao and Y. Liu, ACS Appl. Mater. Interfaces., 2015, 7, 14376−14383.
23 L. Chen, H. Deng, J. Tao, H. Cao, L. Huang, L. Sun, P. Yang and J. Chu, RSC Adv., 2015, 5, 84295–84302.
24 K. Woo, Y. Kim and J. Moon, Energy Environ. Sci., 2012, 5, 5340–5345.
25 K. Zhang, Z. Su, L. Zhao, C. Yan, F. Liu, H. Cui, X. Hao and Y. Liu, Appl. Phys. Lett., 2014, 104, 141101.
26 F. Liu, K. Sun, W. Li, C. Yan, H. Cui, L. Jiang, X. Hao and M.A. Green, Appl. Phys. Lett., 2014, 104, 051105.
27 H. Xin, J.K. Katahara , I.L. Braly and H.W. Hillhouse, Adv. Energy Mater., 2014, 4, 1301823.
28 Y. Cao, M.S. Denny, J.V. Caspar, W.E. Farneth, Q. Guo, A.S. Ionkin, L.K. Johnson, M. Lu, I. Malajovich, D. Radu, H.D. Rosenfeld, K.R. Choudhury and W. Wu, J. Am. Chem. Soc., 2012, 134, 15644−15647.
29 J. Tao, J. Liu, J. He, K. Zhang, J. Jiang, L. Sun, P. Yang and J. Chu, RSC Adv., 2014, 4, 23977–23984.
30 M. Kumar, A. Dubey, N. Adhikari, S. Venkatesan and Q. Qiao, Energy Environ. Sci., 2015, 8, 3134–3159.
31 Y. Lin, S. Ikeda, W. Septina, Y. Kawasaki, T. Harada and M. Matsumura, Sol. Energy Mater. Sol. Cells., 2014, 120, 218–225.
32 G. Yang, Y. Li, B. Yao, Z. Ding, R. Deng, X. Fang and Z. Wei, ACS Appl. Mater. Interfaces., 2015, 7, 16653–16658.
33 L. Guo, Y. Zhu, O. Gunawan, T. Gokmen, V.R. Deline, S. Ahmed, L.T. Romankiw and H. Deligianni, Prog. Photovolt: Res. Appl., 2014, 22, 58–68.
34 T.K. Todorov, J. Tang, S. Bag, O. Gunawan, T. Gokmen, Y. Zhu and D.B. Mitzi, Adv. Energy Mater., 2013, 3, 34–38.
35 K.E. Roelofs, Q. Guo, S. Subramoney and J.V. Caspar, J. Mater. Chem. A, 2014, 2, 13464–13470.
36 D. Kang, T.W. Kim, S.R. Kubota, A.C. Cardiel, H.G. Cha and K.S. Choi, Chem. Rev., 2015, 115, 12839–12887.
37 V.T. Tiong, Y. Zhang, J. Bell and H. Wang, CrystEngComm, 2014, 16, 4306–4313.
38 K. Clauwaert, K. Binnemans, E. Matthijs and J. Fransaer, Electrochimi. Acta, 2016, 188, 344–355.
39 J. Kim, H. Hiroi, T.K. Todorov, O. Gunawan, M. Kuwahara, T. Gokmen, D. Nair, M. Hopstaken, B. Shin, Y.S. Lee, W. Wang, H. Sugimoto and D.B. Mitzi, Adv. Mater., 2014, 26, 7427–7431.
40 S. Bag, O. Gunawan, T. Gokmen, Y. Zhu, T.K. Todorov and D.B. Mitzi, Energy Environ. Sci., 2012, 5, 7060–7065.

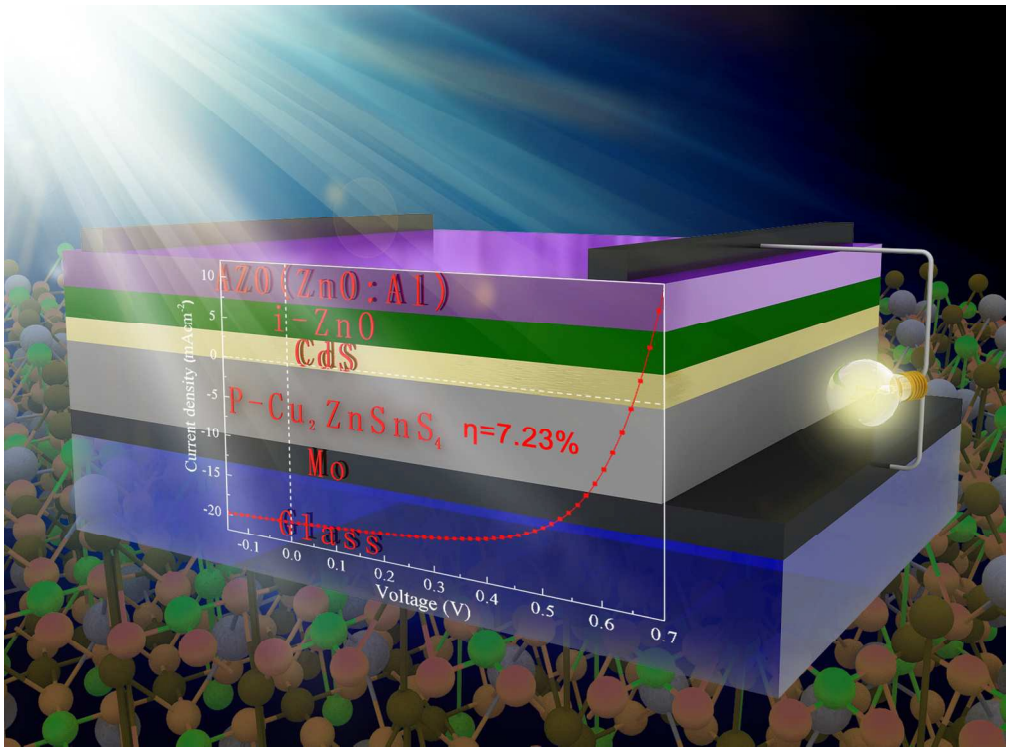

599x443mm (72 x 72 DPI)